Precise columbite-(Fe) and zircon U-Pb dating of the Nanping No. 31 pegmatite vein in northeastern Cathaysia Block, SE China

Tang Yong [a,c], Zhao Jing-Yu [a,b], Zhang Hui [a,*], Cai Da-Wei [a,b], Lv Zheng-Hang [a], Liu Yun-Long [a,b], Zhang Xin [a,b]

[a] Key Laboratory for High Temperature and High Pressure Study of the Earth's Interior, Institute of Geochemistry, Chinese Academy of Sciences, Guiyang 550081, China
[b] University of Chinese Academy of Sciences, Beijing 100049, China
[c] State Key Laboratory of Ore Deposit Geochemistry Chinese Academy of Sciences, Institute of Geochemistry, Chinese Academy of Sciences, Guiyang 550081, China

ABSTRACT

The Nanping pegmatite deposit is a large Ta-Nb-Sn deposit in the northeastern Cathaysia Block, SE China. Columbite-group minerals from zone I in the Nanping No. 31 pegmatite vein belong to columbite-(Fe). The compositions and texture features of zircon grains from the same zone identify their magmatic origin. Columbite-(Fe) U-Pb age coincides well with the U-Pb age of zircon, and these age data constrain the absolute formation timing of this pegmatite vein to approximately 387 Ma. Zircon εHf(t) values from the Nanping No. 31 pegmatite range from −13.81 to −11.60 with the T_{DM2} model ages ranging from 2107 to 2246 Ma, implying that the Nanping pegmatite-forming melts are derived from Paleoproterozoic metasedimentary rocks. The differences in emplacement age and Hf isotopic features preclude the surrounding granites from being the parental granite of the pegmatite vein.

© 2016 Published by Elsevier B.V.

1. Introduction

Granitic Pegmatite is an igneous rock, commonly of granitic composition, that is distinguished from other igneous rocks by its extremely coarse but variable grain-size, or by an abundance of crystals with skeletal, graphic, or other strongly directional growth-habits (Cameron, 1949; Černý, 1991c, 1992; Jahns and Burnham, 1969; Landes, 1933; London, 2008 and references therein). Pegmatites have long attracted interest for the colorful gemstones, fine mineral specimens and rare metal elements (such as Ta, Li, Sn, Be, Cs, Rb, etc.) they contain. A great deal of effort has been made researching the origin, genetic classification, mineralogy and internal structure of pegmatites (e.g., Černý et al., 1985; Černý, 1991b,c; Zhang et al., 2004a,b, 2008; Černý and Ercit, 2005; London, 2005, 2008 and references therein, London, 2009, 2014; Simmons and Webber, 2008; Rao et al., 2009, 2011, 2012, 2014a,b; Dill, 2015 and references therein). The model that states that rare-element pegmatites are a product of crystallization from residual granitic melt is widely accepted. According to this model, rare-element pegmatites should be distributed around the parental granite. Therefore identification of fertile parental granite is an important exploration tool in the search for rare-element pegmatites, because their discovery can greatly reduce the required search area (Selway et al., 2005). However, it is often erroneous

to treat a particular granite as the parental granite based solely on the close spatial relation of pegmatites. In many cases, the rare-metal pegmatites are isolated in time from the granites considered to be parental, with which they are spatially associated (Zagorsky et al., 2014). The same dilemma arises when discussing the geodynamic setting of pegmatites. So far, there is no consensus on the geodynamic factors that control granite-pegmatite systems. Conclusions about the geodynamic settings of so-called parental granites are usually extended to the associated pegmatite. However, due lack of reliable isotopic dating for both groups of rocks, this approach often yields wrong results.

Aldrich et al. (1956) first reported the U-Pb age of coltan (columbite-tantalite group) from the Brown Derby pegmatite, and subsequent research has indicated that the U-Pb dating of coltan is a powerful method for dating coltan-bearing rocks including peraluminous granite, pegmatite, alkaline and carbonatitic intrusions (Romer and Smeds, 1994, 1996, 1997; Romer and Lehmann, 1995; Smith et al., 2004; Baumgartner et al., 2006; Dill et al., 2007; Dewaele et al., 2011; Deng et al., 2013; Che et al., 2015). Zircon is a widely used mineral for isotopic and geochemical studies, due to the high content of trace elements and REEs occurring in its crystalline structure and its strong resistance to erosion, weathering and alteration processes. Owing to the close chemical affinities between Hf and Zr, the element Hf could directly replace the latter in the zircon crystal lattice. This behavior makes Hf more compatible in zircon than the REEs, especially Lu, leading to low Lu/Hf ratios (typically <0.001). For that reason, the

radioactive decay of ^{176}Lu does not significantly change the Hf isotope composition of zircon with time. Moreover, the low intracrystalline diffusion rate of Hf in zircon and the high closure temperature of the Lu-Hf system suggest that the effect of post-crystallization thermal events on the Hf isotope composition is small. Hence, the εHf and T$_{DM}$ model ages may provide reliable and significant information about the magma source. In particular, when coupled with *in situ* U-Pb geochronological data, the isotopic composition may permit characterization of a magmatic event (Cherniak and Watson, 2003; Kinny and Maas, 2003).

In this paper, in order to determine the age of pegmatite emplacement, we performed LA-ICPMS U-Pb dating of coltan and zircon from the Nanping No. 31 pegmatite vein. Zircon Hf isotope is also analyzed, in order to trace the pegmatite-forming melt source. All these data allowed the establishment of temporal relationship between pegmatites and associated granites.

## 2. Geological background

2.1. Regional geology

The Nanping pegmatite district is located in the northeastern portion of the South China Block (SCB). The SCB was formed by amalgamation of the Yangtze and Cathaysia Blocks during the Neoproterozoic along the Jiangshan-Shaoxing Fault (Charvet et al., 1996; Charvet, 2013; Yao et al., 2014, 2015; Yan et al., 2015); then the entire SCB was rifted in response to the breakup of the supercontinent Rodinia during the Late Neoproterozoic, with the period of rifting lasting into the Early Paleozoic (Shu et al., 2011). During the Phanerozoic, the SCB was reworked by three intense tectono-thermal events in the Early Paleozoic, the Early Mesozoic and the Late Mesozoic (Shu et al., 2006, 2008, 2009, 2014, 2015; Faure et al., 2009; Charvet et al., 2010; Charvet, 2013; Song et al., 2015, 2016). The tectono-thermal events occurring during the Early Paleozoic and the Early Mesozoic were mainly related to the intracontinental orogeny triggered by interactions between the Yangtze and Cathaysia continental blocks. Both events resulted in widespread partial melting of continental crust, thus generating large-scale S-type granite with the peak ages in the range of 430–400 Ma and 240–200 Ma (e.g., Wang et al., 2013). The latest

tectono-thermal event is attributed to NW directed subduction of the Pacific Plate beneath East Asia in the Late Mesozoic, and the igneous activities are dated at 140–100 Ma (Shu et al., 2009 and references therein). At least three geodynamic settings, including the Late Neoproterozoic rift, the Early Paleozoic, and the Early Mesozoic intracontinental orogeny, are favorable for the emplacement of pegmatitic rocks according to Dill (2015). Due to lack of precise ages, the geodynamic setting of the Nanping pegmatites is still not known.

2.2. Local geology

The Nanping pegmatite district is located in the northeastern part of the Cathaysia Block (Fig. 1). Four litho-tectonic units can be recognized, including: a Proterozoic basement unit, Upper Neoproterozoic to Ordovician weakly metamorphosed sediments, a sequence of Upper Paleozoic to Lower-Middle Triassic rocks, and Mesozoic-Cenozoic volcanic and sedimentary rocks. Folds and faults are abundant in this area. The folds are mostly developed in the metamorphic basement, with a predominant N-NE strike (Fig. 2).

The high-grade regional metamorphic rocks were considered to represent the Proterozoic basement (Faure et al., 2009). In the study area, the metamorphic rocks are mainly found in the Dikou Formation. The Dikou Formation comprises fine-grained amphibolite facies garnet- and sillimanite-bearing biotite gneiss, schist and quartzite. SHRIMP zircon U-Pb data imply that the Dikou formation formed later than 0.8 Ga and that the metamorphic age should be younger than 604 Ma (Wan et al., 2007). Upper Neoproterozoic (Sinian) to Ordovician lithologies are represented by sandy-muddy marine facies rocks, which underwent sub-greenschist to lower-greenschist metamorphism. The Silurian rocks are lacking in the area (Shu et al., 2014). The Upper Paleozoic to Lower-Middle Triassic sequences are made of a succession of shallow-marine and shore deposits: Upper Devonian conglomerate and sandstone, Carboniferous-Lower Permian carbonate, Upper Permian shale-sandstone with coal beds, and Lower-middle Triassic limestone and siltstone. The thickness is in the range of 2.5–3.0 km (Shu et al., 2006, 2008). The Mesozoic-Cenozoic formations are mainly represented by the terrigenous deposits of intramontane basins (Shu et al., 2009).
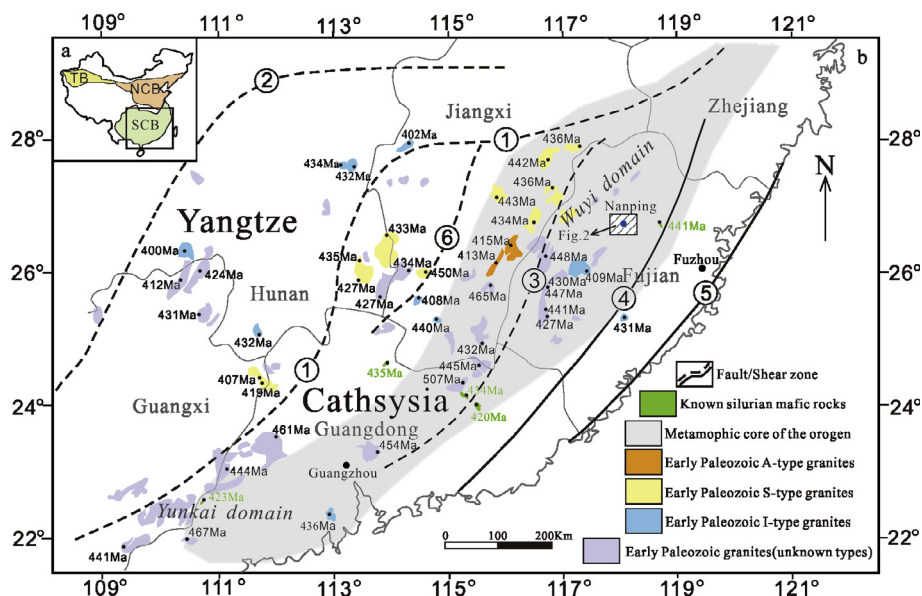
Fig. 1. Geological map showing the distribution of the Early Paleozoic granitic and mafic plutons in the South China Block (modified after Li et al., 2010a, 2010b; Wang et al., 2011; Wang et al., 2013). SCB: South China Block; NCB: North China Block; TB: Tarim Block. Faults: (1) Shaoxing-Jiangshan- Chenzhou-Linwu Fault; (2) Anhua-Luocheng Fault; (3) Heyuan-Guangfeng Fault; (4) Zhenghe-Dapu Fault; (5) Changle-Nan'ao Fault; (6) Ganjiang Fault.
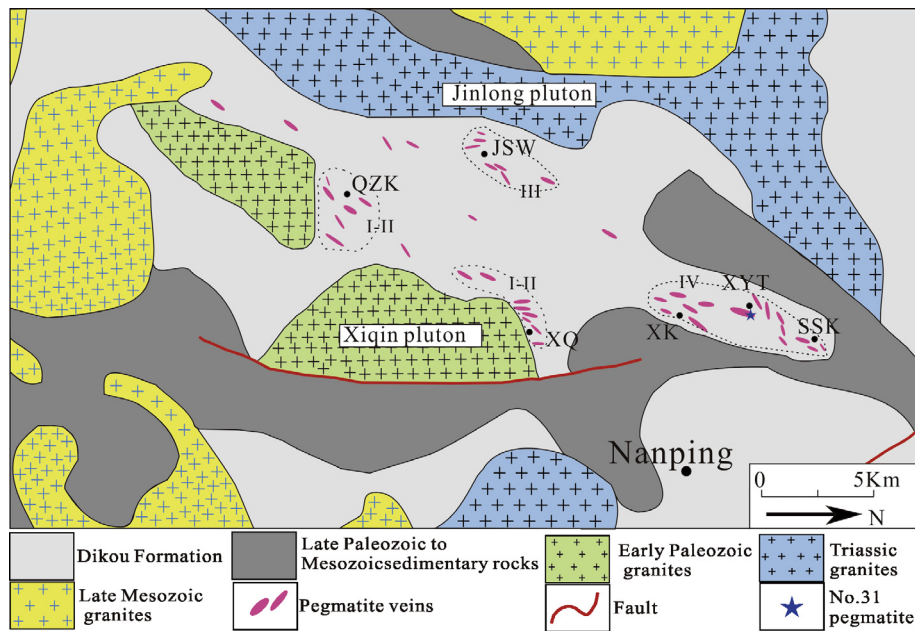
Fig. 2. Simplified geological map of the Nanping pegmatite district (modified after Yang et al., 1987). SSK, XYT, XK, XQ, JSW, and QZK are the abbreviations of Shishunken, Xiyuantou, Xikeng, Xiqin, Jushuwang, and Qiuzhuke, respectively. I, II, III, and IV are the types of pegmatites according to Yang et al., 1987.

The Early Paleozoic (440–400 Ma) and Triassic (240–200 Ma) peraluminous granites are common, responding to the Early Paleozoic and Triassic regional-scale tectono-magmatic events. Late Mesozoic rocks also occur, and this magmatic event is attributed to NW directed subduction of the Pacific Plate beneath East Asia in the Late Mesozoic (Shu et al., 2015, and references therein).

2.3. The Nanping pegmatites

Approximately 500 pegmatite veins, with an outcrop area of approximately 250 km², occur in the Nanping pegmatite district. These pegmatites are limited in distribution to the boundary between the Xiqin granite and Jinlong granite plutons, which are considered to be the parental granites (Fig. 2). Clusters of Nanping pegmatites occur in Shishunken, Xiyuantou, Xikeng, Xiqin, Jushu-

wang, and Qiuzhuke, and intrude into the two-mica schists of the Dikou Formation. The Nanping pegmatites belong to the LCT family (pegmatites enriched in Lithium, Cesium and Tantalum, which are derived from peraluminous s-type granite) (Černý and Ercit, 2005). In LCT pegmatite groups, regional zoning of different pegmatite types and subtypes is commonly observed, and the following spatial sequence of pegmatite categories can be generally outlined in the Nanping pegmatite district (Qiu and Yang, 1985): from muscovite-orthoclase-albite (tabular) pegmatite (type I), muscovite-albite-orthoclase pegmatite (type II), and muscovite-orthoclase-albite (fine grained) pegmatite (type III), to muscovite-albite-spodumene pegmatite (type IV) (following the classification of Yang et al. (1987)), or, from barren, beryl-columbite subtype, and beryl-columbite-phosphate subtype to spodumene or petalite, ±amblygonite subtypes (following the

Table 1
Major types of Nanping granitic pegmatites and their features.

Pegmatite types		Muscovite-K-feldspar-albite (I)	Muscovite-albite-K-feldspar (II)	Muscovite-K-feldspar-albite (III)	Muscovite-albite-spodumene (IV)
Major minerals	Muscovite	5.9 wt.%	15.5 wt.%	10 wt.%	8.7 wt.%
	k-Feldspar	19 wt.%	27 wt.%	13 wt.%	4 wt.%
	Albite	35 wt.% (tabular)	26 wt.%	48 wt.% (fine grained)	40 wt.%
	Quartz	39 wt.%	29 wt.%	26 wt.%	30 wt.%
	Spodumene + montebrasite	Absent	Absent	Few	12 wt.%
Accessory minerals		Tourmaline, spessartine	Spessartine, apatite	Apatite	Apatite, cassiterite, phosphates, nanpingite
Rare metal minerals		Ferrocolumbite, xenotime, monazite	Columbite-tantalite	Columbite-tantalite, beryl, hafnian zircon	Columbite-tantalite, wodginite, tapiolite, microlite, beryl, herderite, hafnian zircon, thoreaulite, pollucite
Internal zoning		Unzoned or weakly zoned		Complex zoned: quartz-muscovite; quartz-albite; quartz-albite-K-feldspar; quartz-K-feldspar	Complex zoned: quartz-muscovite-albite; saccharoidal ablite; cleavelandite-quartz-spodumene; quartz-spodumene-montebrasite; blocky quartz-K-feldspar
Morphology		Dyke; oblique to or parallel with foliation; several to tens of meters in length, and tens of centimeters to several meters in thickness	Dyke; oblique to or parallel with foliation; a few to tens of meters in length, and tens of centimeters to several meters in thickness.	Lenticular shape, dyke; parallel with foliation; a few to a hundred meters in length, and tens of centimeters to several meters in thickness.	Lenticular shape, dyke; parallel with foliation; a few to hundreds of meters in length, and several to thirty meters in thickness.
Wall-rock alteration		Silicification, micatization, tourmalinization	Silicification, tourmalinization	Silicification, micatization, tourmalinization	Silicification, micatization, tourmalinization

paragenetic-geochemical scheme of Černý and Ercit (2005)). The geological and mineralogical features of these pegmatites are summarized in Table 1.

The Nanping No. 31 pegmatite is located in the Xiyuantou area, 8 km west of the city of Nanping. The Nanping No. 31 pegmatite is a type IV pegmatite, and it is the most highly differentiated and well-mineralized pegmatite in the Nanping district. In the past several decades, this pegmatite vein has mainly been mined for Nb-Ta-oxides, as it is a large-size rare metal deposit with 0.028 wt% Ta_2O_5, 0.016 wt% Nb_2O_5, and 0.068 wt% Sn. The No. 31 pegmatite is a lenticular body with a predominant N-NE orientation, which is steeply intruded into schists (Fig. 3a), and is 5–6 m in thickness, 90 m in depth, and 300–600 m in length. Fig. 3b shows the different zones observed in the open pit at a depth of 515 m, which comprises roughly five discontinuous zones from the outermost zone inward as follows. Zone I is mainly composed of medium-grained quartz, muscovite and fined-grained albite. Other minerals include cassiterite, columbite-tantalite-group minerals, zircon, beryl, hurlbutite, phenakite, fluorapatite, and strontiohurlbutite. Zone II typically contains saccharoidal albite and greenish muscovite. This zone can be further subdivided into facies IIa (saccharoidal albite >90 vol %, greenish muscovite <10 vol%) and facies IIb (60 vol% greenish muscovite with 10 vol% quartz and 30 vol% albite). Cassiterite, columbite-tantalite-group minerals, wodginite-group minerals and tapiolite-(Fe), are mainly concentrated at the boundary between the two facies. Other accessory minerals are beryl, phenakite, hydroxyherderite, hurlbutite, euclase, strontiohurlbutite and fluorapatite. Zone III is characterized by platy crystals of albite (variety "cleavelandite"), coarse quartz and spodumene. Columbite-tantalite-group minerals, wodginite-group minerals, tapiolite-(Fe), microlite, zircon, cassiterite, fluorapatite, amblygonite–montebrasite and beryl are present as accessory minerals. Zone IV (intermediate unit) contains coarse-grained quartz, massive spodumene, and montebrasite crystals. Accessory minerals include columbite-group minerals, wodginite-group minerals, tapiolite-(Fe), microlite-group minerals, beryl, cassiterite, pollucite, lazulite and strontiohurlbutite. Massive montebrasite

crystals in this zone are frequently altered to secondary phosphate minerals: palermoite, bertossaite, kulanite and hydroxylapatite. Finally, most of the spodumene crystals in zones III and IV have been completely altered to fine-grained white mica assemblages. Zone V (quartz core) in the pegmatite core consists of blocky quartz and K-feldspar, and accessory minerals are very rare.

3. Analytical methods

3.1. Zircon major elements, U-Pb dating and Hf isotope analysis

Zircons were separated by heavy liquid and magnetic separation methods. Pure zircons were handpicked under a binocular microscope, then mounted in epoxy resin and polished until the grain interiors were exposed. The cathodoluminescence (CL) images were obtained using a JSM6510 scanning electron microscope, manufactured by the JEOL Corporation (Japan), at the Beijing zircon dating navigation technology limited company.

3.1.1. Major elements

Zircon major element compositions were determined at the State Key Laboratory of Geological Processes and Mineral Resources, China University of Geosciences (Wuhan), using a JEOL 8100 electron probe micro-analyzer equipped with four wavelength-dispersive spectrometers (WDS). EMPA was operated at an accelerating voltage of 15 kV and a beam current of 20 nA. The beam diameter was ca. 1 μm. Peaks and backgrounds for all elements were measured with counting times of 30 and 15 s. The following standards were used for quantitative elemental analyses: zircon (Zr, Si), Hf metal (Hf), UO_2 (U), ThO_2 (Th), apatite (P), YPO_4 (U), topaz (Al) and hornblende (Fe, Ca). All data were reduced using the ZAF correction program.

3.1.2. Zircon trace element compositions and U-Pb dating

Zircon U-Pb isotopes and trace elements were simultaneously determined by an Elan DRC-e ICP-MS coupled with a GeoLasPro 193 nm Laser-Ablation System at the State Key Laboratory of Ore
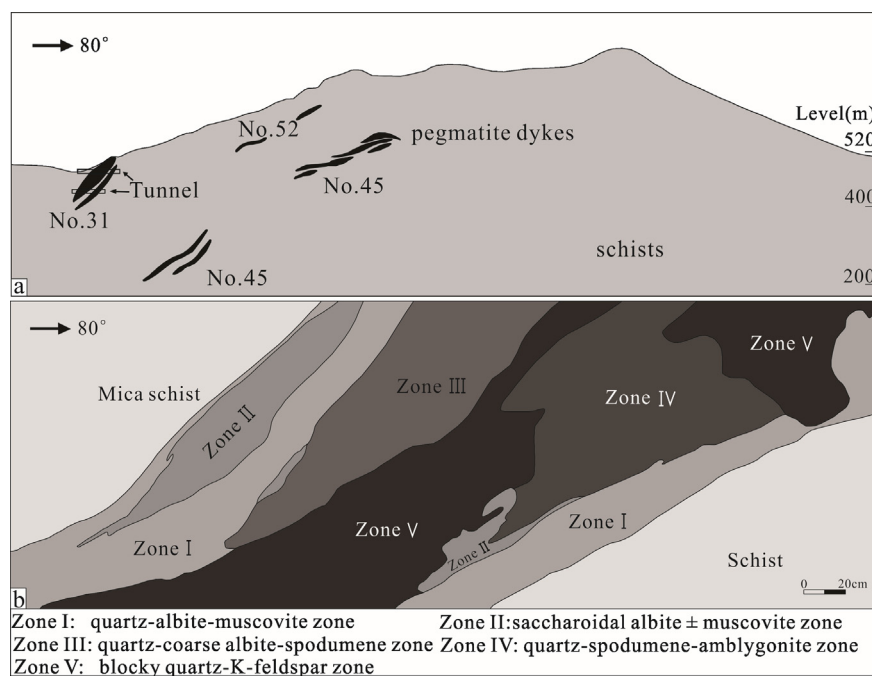

Fig. 3. The Profile (a) and internal textural zones (b) of the Nanping No. 3 granitic pegmatite vein (modified after Yang et al., 1987).

Deposit Geochemistry, Institute of Geochemistry, Chinese Academy of Sciences (CAS), Guiyang. Detailed analytical procedure and conditions were described by Yuan et al. (2008). The conditions were as following: laser frequency of 8 Hz with an energy of 34–40 mJ, beam diameter of 30 μm, background acquisition of 30 s and signal acquisition of 60 s. Helium was used as a carrier gas to transport the ablated materials from the laser-ablation cell to the ICP-MS torch. Zircon 91500 was used as an external standard to normalized isotopic discrimination. Trace elements concentrations were calibrated by using ^{29}Si as internal calibrant and NIST610 glass as reference material. Raw data were processed using the ICPMSDataCal program (Liu et al., 2008). Uncertainties of individual analyses are reported with 1σ errors; weighted mean ages were calculated at 1σ confidence level. Common Pb correction used the ^{204}Pb methods of Andersen (2002). The weighted mean U-Pb ages and Concordia plots were processed using ISO-PLOT software (Ludwing, 2003).

3.1.3. Zircon Lu-Hf isotope

In-situ Hf isotope analyses were conducted at the State Key Laboratory of Geological Processes and Mineral Resources, China University of Geosciences (Wuhan), using a Neptune Plus MC-ICP-MS (Thermo Fisher Scientific, Germany) in combination with a Geolas 2005 excimer ArF laser ablation system (Lambda Physik, Göttingen, Germany). The analyses were carried out with a spot size of 44 μm and a repetition rate of 5 Hz. Each measurement consisted of 20 s of acquisition of the background signal followed by 50 s of ablation signal acquisition. Detailed operating conditions for the laser ablation system and the MC-ICP-MS instrument and analytical method are the same as described by Hu et al. (2012). Zircon standard 91500 was used to monitor the analytical accuracy and, yielded a weighted mean $^{176}Hf/^{177}Hf$ ratio of 0.282316 ± 0.000006 (2σ, n = 30). The decay constant (λ) of 1.867×10^{-11} year^{-1} was adopted for ^{176}Lu (Söderlund et al., 2004), and $\varepsilon Hf(t)$ values were calculated using the present-day chondritic values of $^{176}Hf/^{177}Hf_{CHUR(0)} = 0.282772$ and $^{176}Lu/^{177}Hf_{CHUR(0)} = 0.0332$ (Blichert-Toft and Albarède, 1997). Depleted mantle model ages (T_{DM}) were calculated with reference to the depleted mantle at a present-day $^{176}Hf/^{177}Hf$ ratio of 0.28325 and $^{176}Lu/^{177}Hf$ of 0.0384 (Griffin et al., 2002). The Hf isotope crustal model ages (T_{2DM}) were calculated by assuming that parental magma has been derived from an average continental crust, with $^{176}Lu/^{177}Hf = 0.015$.

3.2. Coltan major element compositions and U-Pb dating

The coltan grains were extracted, mounted in epoxy resin, and polished by standard methods. The back-scattered electron images (BSE) were obtained using a JEOL JXA-8100M electron probe micro-analyzer (EMPA) at the State Key Laboratory for Mineral Deposits Research at Nanjing University, to ensure that the targets of Fe-columbite for subsequent in situ analyses are fresh and without inclusions and cracks.

3.2.1. Coltan major element compositions

Coltan major elements were analyzed at Nanjing University using the afore-mentioned EMPA equipped with four wavelength-dispersive spectrometers (WDS). EMPA was operated at an accelerating voltage of 15 kV and a beam current of 20 nA. The beam diameter was ca. 1 μm. Peaks and backgrounds for all elements were measured with counting times of 20 and 10 s, respectively. The following standards were used: Nb metal (Nb), Ta metal (Ta), Sc metal (Sc) cassiterite (Sn), fayalite (Fe), and MnTiO₃ (Ti, Mn). All data were reduced using the ZAF correction program.

3.2.2. Coltan U-Pb dating

Coltan U-Pb isotopic analyses were determined at the Institute of Geology and Geophysics, Chinese Academy of Sciences, using a Geolas PLUS 193 nm excimer ArF laser ablation system coupled with an Agilent 7500a quadrupole-based, inductively coupled plasma mass spectrometer (Q-ICP-MS). The detailed analytical procedures are similar to that described by Che et al. (2015). During laser ablation, a NIST SRM 610 reference material glass was used to optimize the instrumental parameters. Using 91500 zircon as an external standard, GJ-1 zircon standard (608.5 ± 0.4 Ma, Jackson et al., 2004) was used to check the analytical accuracy. In each routine analysis, every 5 sample analyses were followed by two zircon standards (91500 and GJ-1), one coltan standard (Coltan 139) and one NIST SRM 610 measurement. Each spot analysis consists approximately of 30 s background acquisition, 60 s sample data acquisition and up to 60 s gas blank for flashing sample. The fractionation correction and U-Pb ages were calculated using GLITTER 4.0 (GEMOC, Macquarie University). The concordia and weighted mean U-Pb ages were calculated using the ISOPLOT/EX 3.23 software package.

4. Results

4.1. Zircon

The results of zircon U-Pb dating and major composition are listed in Tables 2 and 3, respectively. Two groups of zircon from Zone I in Nanping No. 31 pegmatite were identified (Fig. 4a). Group I is colorless, transparent, and long prismatic in morphology, with length varying from ~50 to 100 μm and elongation (length-to-width) ratios of 2:1 and 3:1. As shown by CL images, these grains exhibit well-developed oscillatory zoning. Four spots were analyzed on four grains of this group. These grains have relatively low contents of Th (749–295 ppm) and U (514–1540 ppm), and high Th/U ratios (0.49–1.56). The four grains give apparent $^{206}Pb/^{238}U$ ages ranging from 828.5 ± 10.7 Ma to 905.0 ± 9.9 Ma (Fig. 5a). These ages are consistent with the formation ages of the original volcano-sedimentary sequence of the Dikou Formation. Therefore, the zircons are interpreted as grains captured during the ascent of the magma or inherited from a source.

Group II is light brown, semitransparent, and stubby in morphology, with length in the range of 50–100 μm and elongation ratios of approximately 1:1. In CL images, these crystals display relatively homogeneous internal textures. The major compositions of these zircons are shown in Table 3. These grains contain 31.42–34.51 wt% SiO_2, 55.27–64.33 wt% ZrO_2, 1.12–11.34 wt% HfO_2, and are characterized by very low concentrations of non-formula elements (e.g., Ca, Al, and Fe). Chemically, these grains are typical of normal crystalline Hf-rich zircons.

Group II zircon crystals exhibit the similar REE features to Group I. All these grains have highly variable $\sum$REE abundances that vary from 1000 to 3200 ppm (Table 4). The chondrite-normalized REE patterns of these zircon grains are characterized by a steeply-rising slope from La to Lu with positive Ce and negative Eu anomalies (Fig. 6a).

A total of fourteen spots were analyzed on fourteen grains from Group II. The zircon grains were characterized by extremely low Th (3.6–40.3 ppm) and high U (6193.5–17815.7 ppm) concentrations. Although the zircons contain high contents of U, they have no fractures and low concentrations of non-formula elements, indicating that the effects of the metamictization and alteration by later fluids on the zircons are very weak. Given that four of the fourteen spots give apparent $^{206}Pb/^{238}U$ ages that are nearly the same as the others, the variable discordance possibly reflects some Pb loss and, therefore, they are discarded as statistical outliers. The

Table 2
LA-ICP-MS zircon U-Pb analytical results of the Nanping No. 31 pegmatite.

| No.	Pb (ppm)	Th (ppm)	U (ppm)	$^{207}Pb/^{206}Pb$ Ratio	1σ	$^{207}Pb/^{235}U$ Ratio	1σ	$^{206}Pb/^{238}U$ Ratio	1σ	$^{207}Pb/^{206}Pb$ Age (Ma)	1σ	$^{207}Pb/^{235}U$ Age (Ma)	1σ	$^{206}Pb/^{238}U$ Age (Ma)	1σ
Zir-01	619.3	4.1	12947.9	0.0571	0.0008	0.4895	0.0161	0.0619	0.0003	494.5	29.6	404.6	10.9	387.1	2.1
Zir-02	149.8	362.0	615.3	0.0683	0.0016	1.4236	0.0537	0.1507	0.0018	875.9	48.1	898.9	22.5	905.0	9.9
Zir-03	564.9	4.0	12245.9	0.0540	0.0005	0.4635	0.0148	0.0619	0.0003	372.3	22.2	386.7	10.3	387.2	2.0
Zir-04	249.1	2.0	4402.0	0.0715	0.0016	0.6153	0.0263	0.0620	0.0005	972.2	46.3	486.9	16.5	387.5	3.2
Zir-05	465.1	40.3	9697.6	0.0855	0.0210	0.5028	0.0210	0.0620	0.0005	1325.6	486.3	413.6	14.2	387.9	3.1
Zir-06	184.0	645.7	614.7	0.0660	0.0019	1.2455	0.0556	0.1371	0.0019	807.1	60.0	821.4	25.1	828.5	10.7
Zir-07	601.5	13.0	11538.2	0.0643	0.0015	0.5526	0.0217	0.0619	0.0003	750.0	48.1	446.7	14.2	387.2	1.6
Zir-08	832.1	19.6	17815.7	0.0558	0.0005	0.4786	0.0147	0.0619	0.0004	455.6	18.5	397.1	10.1	387.2	2.6
Zir-09	454.3	3.6	9832.3	0.0541	0.0005	0.4627	0.0143	0.0619	0.0003	372.3	20.4	386.1	9.9	387.4	2.1
Zir-10	302.9	7.2	6193.5	0.0596	0.0010	0.5129	0.0187	0.0621	0.0010	590.8	39.8	420.4	12.5	388.4	5.8
Zir-11	379.1	122.1	7132.5	0.0905	0.0254	0.5669	0.0174	0.0630	0.0007	1436.7	559.4	456.0	11.3	393.9	4.4
Zir-12	530.5	9.5	11198.2	0.0572	0.0007	0.4899	0.0133	0.0620	0.0003	501.9	27.8	404.8	9.0	387.7	1.8
Zir-13	595.4	5.8	11541.8	0.0629	0.0007	0.5384	0.0148	0.0619	0.0005	705.6	22.2	437.4	9.8	387.4	2.7
Zir-14	408.4	7.0	8926.2	0.0577	0.0007	0.4931	0.0156	0.0619	0.0006	516.7	21.3	407.0	10.6	387.0	3.4
Zir-15	320.9	748.6	1539.8	0.0677	0.0012	1.3343	0.0460	0.1425	0.0010	857.4	37.5	860.8	20.0	858.7	5.7
Zir-16	177.0	697.8	446.0	0.0723	0.0031	1.4110	0.0688	0.1421	0.0015	994.4	87.0	893.6	29.0	856.4	8.6
Zir-17	652.3	5.8	14144.0	0.0547	0.0006	0.4693	0.0139	0.0619	0.0003	466.7	28.7	390.7	9.6	387.4	1.8
Zir-18	491.9	13.8	10509.5	0.0543	0.0007	0.4656	0.0174	0.0619	0.0003	388.9	27.8	388.2	12.1	387.4	2.1
Zir-19	321.6	294.9	513.8	0.1575	0.0025	8.0598	0.2818	0.3696	0.0035	2429.3	26.2	2237.8	31.6	2027.4	16.4

Table 3
Major element compositions of zircon from the Nanping No. 31 pegmatite.

| Oxide	1	2	3	4	5	6	7	8	9	10	11	12	13	14	15	16	17	18	19	20
SiO₂	34.51	33.67	34.29	33.76	33.57	33.49	31.42	33.48	33.12	32.22	33.84	34.04	34.06	34.08	34.38	33.71	32.98	33.48	33.71	34.11
ZrO₂	59.88	56.09	60.62	59.76	64.20	64.22	60.87	60.52	61.04	55.27	58.82	60.34	59.81	63.52	64.33	60.18	61.77	61.59	61.62	63.91
HfO₂	6.37	9.41	4.64	5.16	1.44	1.84	5.86	4.75	4.90	11.34	6.57	4.53	4.71	1.27	1.12	5.62	4.82	4.70	4.58	1.33
UO₂	0.17	0.06	0.76	0.67	0.04	0.02	0.37	0.54	0.25	0.34	0.18	0.42	0.33	0.16	0.15	0.39	0.84	0.65	0.57	–
ThO₂	–	0.09	–	–	–	0.13	0.04	0.04	0.12	0.05	0.04	–	0.02	–	0.09	0.10	–	–	0.01	0.07
Al₂O₃	0.04	0.01	0.01	–	–	–	0.04	–	0.01	–	0.01	–	0.03	0.01	–	–	–	–	–	–
Y₂O₃	–	–	–	–	–	–	–	–	–	–	–	–	–	0.19	0.01	–	–	–	–	–
CaO	–	–	0.02	–	–	0.02	0.01	–	–	0.01	0.01	–	0.04	0.01	–	–	–	–	–	0.04
FeO	0.02	–	–	–	–	0.01	–	–	–	–	0.03	–	0.04	–	–	0.02	0.02	0.02	0.01	0.03
P₂O₅	–	–	–	–	–	–	–	–	–	–	–	–	–	–	–	–	–	–	–	–
Total	100.97	99.33	100.35	99.36	99.25	99.73	98.61	99.33	99.44	99.23	99.50	99.34	99.03	99.24	100.08	100.01	100.44	100.44	100.50	99.48

Structural formula calculated on the basis of O = 6 atoms

apfu	1	2	3	4	5	6	7	8	9	10	11	12	13	14	15	16	17	18	19	20
Si	1.052	1.056	1.049	1.046	1.028	1.025	0.999	1.039	1.029	1.031	1.050	1.050	1.053	1.040	1.040	1.041	1.020	1.030	1.034	1.038
Zr	0.890	0.858	0.904	0.903	0.959	0.958	0.944	0.915	0.925	0.862	0.890	0.907	0.901	0.945	0.949	0.906	0.931	0.924	0.922	0.949
Hf	0.055	0.084	0.040	0.046	0.013	0.016	0.053	0.042	0.043	0.104	0.058	0.040	0.042	0.011	0.010	0.049	0.043	0.041	0.040	0.012
U	0.001	–	0.005	0.005	–	–	0.003	0.004	0.002	0.002	0.001	0.003	0.002	0.001	0.001	0.003	0.006	0.004	0.004	–
Th	–	0.001	–	–	–	0.001	–	–	0.001	–	–	–	–	–	0.001	0.001	–	–	–	–
Al	0.001	–	–	–	–	–	0.002	–	–	–	–	–	0.001	–	–	–	–	–	–	–
Y	–	–	–	–	–	–	–	–	–	–	–	–	–	0.003	–	–	–	–	–	–
Ca	–	–	0.001	–	–	0.001	–	–	–	–	–	–	0.001	–	–	–	–	–	–	0.001
Fe	–	–	–	–	–	–	–	–	–	–	0.001	–	0.001	–	–	0.001	0.001	0.001	–	0.001
P	–	–	–	–	–	–	–	–	–	–	–	–	–	–	–	–	–	–	–	–
Hf#	0.06	0.09	0.04	0.05	0.01	0.02	0.05	0.04	0.04	0.11	0.06	0.04	0.04	0.01	0.01	0.05	0.04	0.04	0.04	0.01

Dash (–) denotes below the detection limit. Hf# = molar Hf/(Zr + Hf)
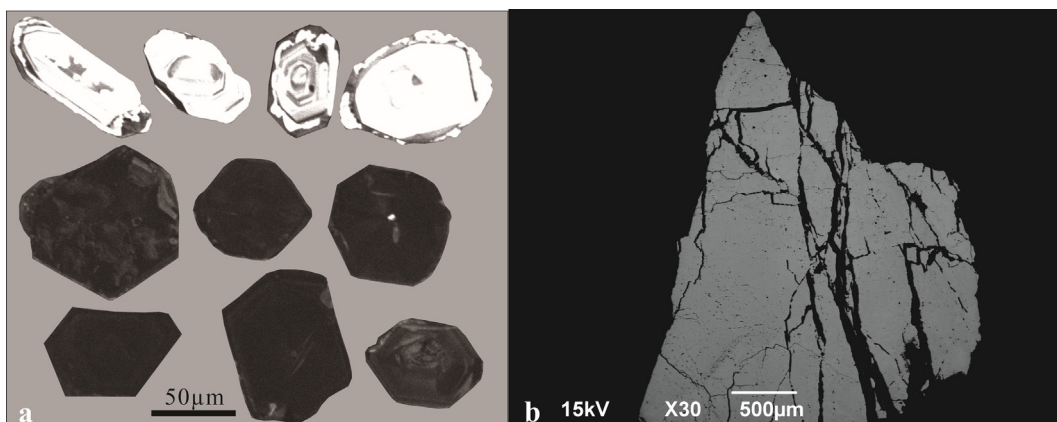
Fig. 4. (a) Representative cathodoluminescence (CL) images of zircons and (b) Back-scattering images of columbite-(Fe).
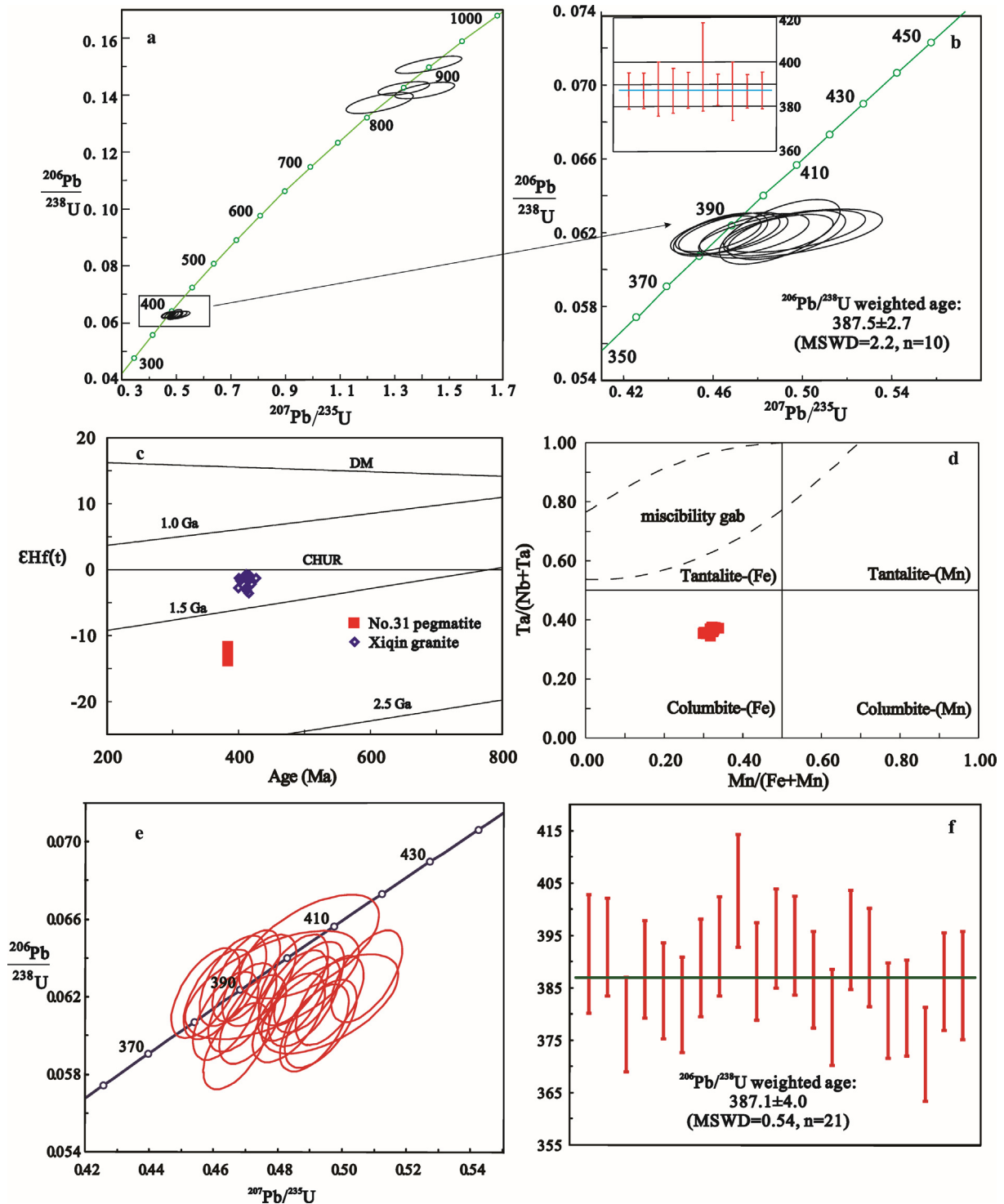
Fig. 5. (a) and (b) U-Pb dating of zircons from the Nanping No. 31 pegmatite vein; (c) Age vs. zircons $\varepsilon_{Hf}(t)$, DM: depleted mantle; CHUR: Chondritic uniform reservoir; 1.0 Ga, 1.5 Ga and 2.5 Ga are the representative of Hf isotope evolution paths for newly generated crust at 1.0 Ga, 1.5 Ga and 2.5 Ga, respectively; (d) the composition of the Columbite-(Fe) in the columbite quadrilateral diagram; (e) and (f) U-Pb dating of columbite-(Fe).

remaining analyses yield a weighted mean $^{206}Pb/^{238}U$ age of 387.5 ± 2.7 Ma (Fig. 5b), and this age is considered to be the initial crystallization age of the pegmatite.

The zircons that were dated with U-Pb were selected for Lu-Hf isotope analyses. Nine spots yielded $^{176}Hf/^{177}Hf$ values of 0.282141 to 0.282206, and the calculated $\varepsilon_{Hf}(t)$ values ranged from −13.81 to −11.60. The Hf isotopic model ages (T_{DM2}) vary mostly between 2107 and 2246 Ma (Table 5, Fig. 5c).

4.2. Columbite-(Fe)

The back-scattered images show that the coltan samples are homogenous, without inclusions, although cracks are highly developed (Fig. 4b). The results of the columbite-(Fe) composition and U-Pb dating are listed in Tables 6 and 7. All of the EMPA analyses plot within the ferro-columbite field (Fig. 5d), with a nearly constant Ta/(Nb + Ta) atomic ratio (0.30–0.34) and Mn/(Mn + Fe)

Table 4
Rare earth elements compositions of zircon from the Nanping No. 31 pegmatite (ppm).

No.	Zir-01	Zir-02	Zir-03	Zir-04	Zir-05	Zir-06	Zir-07	Zir-08	Zir-09	Zir-10	Zir-11	Zir-12	Zir-13	Zir-14	Zir-15	Zir-16	Zir-17	Zir-18	Zir-19
La	0.06	0.00	0.33	0.02	0.05	0.07	0.36	0.15	0.04	1.72	0.07	1.27	0.05	0.87	0.03	0.49	0.09	0.10	0.02
Ce	74.49	57.30	34.31	33.47	49.77	40.67	40.49	43.46	58.23	30.32	56.07	39.93	43.80	69.56	74.06	73.15	44.59	70.08	22.94
Pr	0.28	0.15	1.35	0.28	0.23	0.49	0.48	0.34	0.31	0.59	0.22	1.85	0.94	2.09	0.25	4.11	1.37	0.39	0.37
Nd	5.11	3.15	15.51	4.18	2.10	10.30	6.26	5.73	7.49	4.86	3.90	23.50	13.13	28.23	4.78	36.02	19.36	7.39	6.80
Sm	10.05	6.57	24.17	7.84	8.61	17.64	11.50	8.60	18.12	9.52	11.39	30.68	22.64	34.67	14.09	40.76	26.93	12.35	14.84
Eu	0.88	0.31	7.80	1.50	0.26	2.65	1.71	1.65	3.57	1.33	0.55	4.87	4.23	7.28	0.43	4.50	2.90	1.16	2.39
Gd	55.19	40.76	98.03	34.17	51.94	79.92	52.40	40.91	81.30	42.59	62.33	122.94	108.81	149.83	82.85	165.13	109.73	62.76	75.71
Tb	17.65	14.62	27.07	10.63	19.16	23.08	15.58	13.02	24.50	13.09	21.20	33.33	30.38	43.55	30.16	45.58	30.56	18.79	23.02
Dy	205.66	188.83	279.62	124.26	247.59	259.13	177.91	143.93	264.20	152.33	258.85	354.27	331.75	479.28	385.18	506.73	344.03	216.47	267.12
Ho	74.40	69.05	90.41	41.86	92.76	85.42	59.91	50.44	87.54	51.56	94.01	112.79	107.64	156.76	139.16	161.56	114.51	72.90	90.66
Er	336.38	326.23	382.23	193.30	441.76	368.25	276.11	229.87	373.24	233.14	435.59	471.51	442.03	673.28	639.65	677.66	503.03	331.13	389.37
Tm	65.48	65.06	70.31	37.68	89.45	68.39	52.87	44.81	70.44	45.24	86.51	86.42	82.20	123.32	126.69	120.39	91.57	64.07	75.14
Yb	664.27	666.51	690.23	400.44	926.87	699.45	541.86	468.67	708.37	475.22	893.55	839.61	804.65	1238.24	1297.22	1199.73	934.17	686.49	740.95
Lu	110.83	113.33	117.61	69.80	152.42	114.07	91.51	80.49	115.98	81.10	148.06	135.99	134.28	203.59	207.06	190.54	148.87	108.50	119.18

atomic ratio (0.35–0.38). These crystals also contain minor amounts of SnO (0.13–0.54 wt%), TiO_2 (0.29–0.43 wt%) and Sc_2O_3 (0.07–0.32 wt%).

A total of twenty spots were analyzed, and these analyses cluster as a tight coherent group on the concordia curve, yielding a weighted mean $^{206}Pb/^{238}U$ age of 387.1 ± 4.0 Ma (Fig. 5e, f). The columbite-(Fe) U-Pb age is in fairly good agreement with the zircon U-Pb age, placing the formation timing of the pegmatite at approximately 387 Ma.

5. Discussion

5.1. Zircon: magmatic vs. hydrothermal origin?

Firstly, evidence of aqueous vapor phase saturation at that onset of pegmatite crystallization is lacking yet (London, 2008 and references therein). With regard to Nanping No. 31 pegmatite vein, the complex internal textures of Nb-Ta-Sn oxide minerals from the zones IV–V indicate a distinctly fluid-rich environment at the late stage of crystallization; in contrast, the minerals from zone I to III are characterized by the fractional crystallization of the melt (Rao et al., 2009). Therefore, zircon grains in zone I should have crystallized from melt.

Secondly, it has been proved by experiments that zircon, especially metamict zircon, can be easily altered by external fluid. The alteration zones are commonly characterized by a lowered Th/U ratio, transgressive boundaries with primary zircon, and lowered U-Pb ages. Two processes, diffusion-reaction process and coupled dissolution-reprecipitation process, are proposed to account for the textural and chemical characteristics of re-equilibrated zircon domains (Geisler et al., 2007). On the one hand, non-formula elements, such as Ca, Al, Fe, Mn, and possibly common Pb are gains in diffusion-reaction process. As a result, zircons that interacted with fluids should be characterized by high concentration of non-formula elements. On the other hand, micrometer-sized pores and inclusions of uranium, thorium and/or yttrium phases develop in the dissolution-reprecipitation process. Zircons from zone I in Nanping No. 31 pegmatite has a normal oxide totals (∼ 100 wt%), characterized by low non-formula elements, has Si and Zr contents typical of normal crystalline Hf-rich zircon, and lack pores and mineral inclusions. All features imply that these zircon grains have not been altered by fluid.

Thirdly, as shown in Fig. 1a, chondrite-normalized REE patterns for zircon grains from zone I are characterized by a steeply-rising slope from La to Lu with a positive Ce anomaly and negative Eu anomaly, similar to the other zircons from crustal-source rocks (Hoskin and Schaltegger, 2003). Furthermore, as shown by the discrimination plots for magmatic and hydrothermal zircon

(Fig. 6b and c), the Nanping No. 31 pegmatite zircon compositions plot on or near the fields defined by magmatic zircons.

All the features identify the magmatic origin of these zircon grains. Therefore, the U-Pb ages and Hf isotopic compositions obtained from these zircon crystals are reliable.

5.2. The Nanping pegmatites genesis

Because of the close spatial relation with the Nanping pegmatites, the Xiqin and Jinlong granite pluton were considered to be the parental granites of these pegmatites. The columbite-(Fe) U-Pb age coincides well with the U-Pb age of zircon in the Nanping No. 31 pegmatite vein, and the result constrains the absolute formation timing of this pegmatite vein at approximately 387 Ma. This result implies that the formation of the Nanping pegmatites is related to the Early Paleozoic intracontinental orogeny.

This age is 170 Ma older than that of the Jinlong granite pluton (ca. 220 Ma, our unpublished data), and the time gap between them is so great that a genetic relationship is unlikely to exist. Recently, the emplacement age of the Xiqin granite pluton has been determined, and the LA-ICPMS zircon U-Pb dating yields a weighted mean $^{206}Pb/^{238}U$ age of ca. 410 Ma (Cai et al., 2016). The close temporal and spatial relationship between Xiqin granite pluton and the No. 31 pegmatite seemingly suggest a genetic link between them. However, the εHf(t) values of zircons from the Nanping No. 31 pegmatite are in the range of −13.81 to −1160 with T_{DM2} model ages ranging from 2107 to 2246 Ma, whereas zircon εHf(t) values of the Xiqin granites mainly vary from −0.4 to −3.1 and yield Mesoproterozoic T_{DM2} (Hf) age (mainly ranging from 1.29 to 1.45 Ga) (Cai et al., 2016). The differences in εHf(t) and model ages demonstrate that the Xiqin granite was not the parental granite of the Nanping pegmatites.

LCT pegmatites are usually associated with peraluminous granites (Černý, 1991a). Two extreme cases of granite-pegmatite systems occur in the early Paleozoic orogen in the South China Block (SCB) and the Chinese Altay orogen. Large volumes of Paleozoic granites are confirmed in the SCB, and these granites were emplaced from 390 to 467 Ma, mostly between 430 and 400 Ma (Wang et al., 2011; Zhang et al., 2012; Wang et al., 2013 and references therein). This systematically postdates the peak metamorphism (earlier than 445 Ma, Li et al., 2010a,b) and implies that these rocks were formed in the late- to post-orogenic extensional environment. With the exception of a few I-type granites, most early Paleozoic granites are peraluminous S-type granites. Compared to these late- to post-orogenic S-type granites, the number and volume of outcropping LCT pegmatites are rare in the SCB. In contrast, more than 100,000 granitic pegmatite veins are exposed in the Chinese Altai orogen and these pegmatites predom-
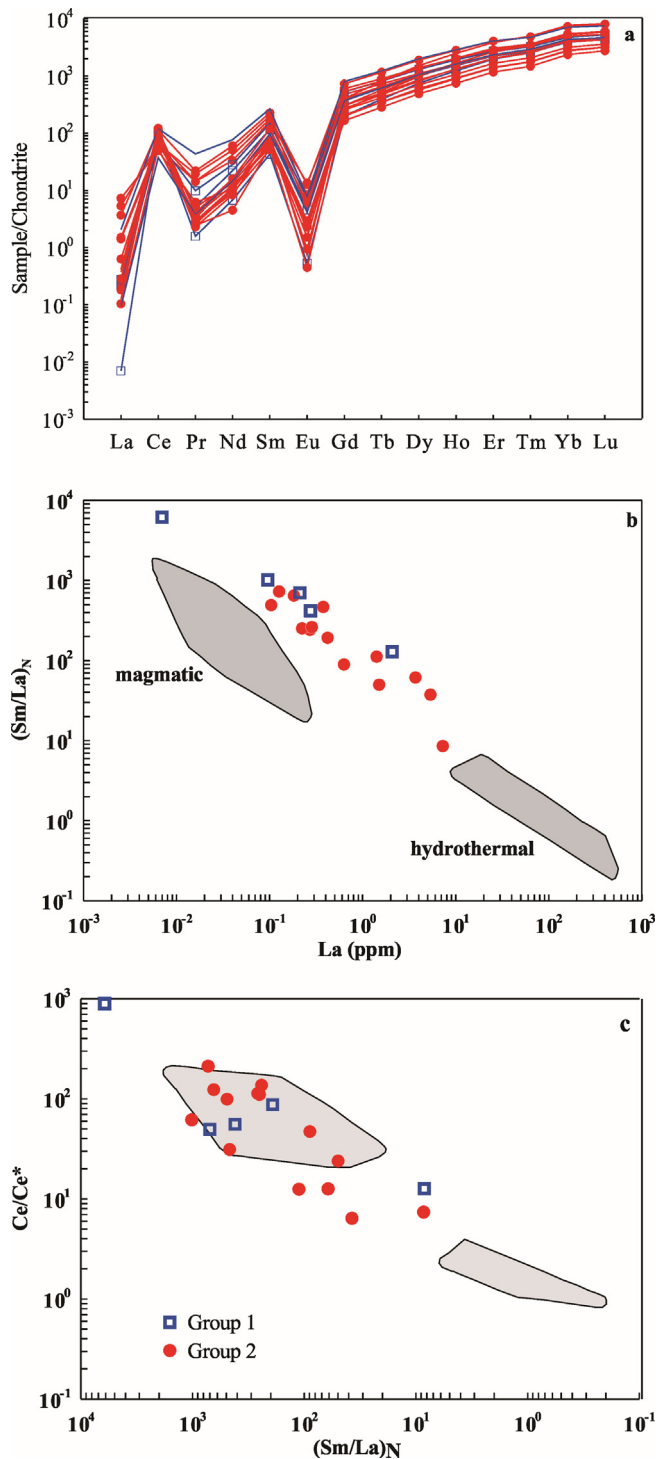
Fig. 6. (a) Chondrited-normalized REE patters for zircons; (b) and (c) Discrimination plots for magmatic and hydrothermal zircon (modified from Hoskin (2005)). All data are normalized to chondrite values of (McDonough and Sun, 1995).

inately belong to LCT family. Recent research has shown that these pegmatites were mainly emplaced from Late Permian to Triassic (Wang et al., 2007; Chen, 2011; Ren et al., 2011; Lv et al., 2012; Ma, 2014). However, just three Mesozoic plutons are identified in the Chinese Altai orogeny: Ala'er I-type granite (ca. 220), Shangkelan I-type granite (ca. 203), and Jiangjunshan A-type granite (ca. 151) (Wang et al., 2014).

Based on different pegmatite genetic models, there are two possibilities to account for the decoupling of the LCT pegmatites and

peraluminous S-type granites. One possibility is that the exposure of LCT pegmatites is related to the erosion level. Granitic pegmatites are generally acknowledged to form by a process of fractional crystallization of granitic melts. A trend of pegmatite intrusion upwards from parental granites is rather frequent under this condition (Černý, 1991b). The present erosion surface may expose either the roots (the parental granite flanked by few pegmatites, with most of the pegmatite aureole eroded away), or the top of the system (the pegmatite aureole alone, with the granitic source remaining hidden). Thus, the former may be the tectonic environment specific for the early Paleozoic orogen in the SCB, and the latter for the Chinese Altay orogen.

A recent study shows that detrital zircons, which come from Late Triassic-Early Cretaceous clastic sedimentary rocks of Mesozoic basins in central southeastern South China, yield an age population of ca. 430 Ma (Meng et al., 2015). The ca. 430 Ma zircons from the Late Triassic-Mid Jurassic to the upper part of the Early Jurassic rocks share remarkable similarities in their Hf isotope characteristics, which is consistent with that of early Paleozoic granite rocks in the Cathaysia blocks (Meng et al., 2015). Therefore, the ca. 430 Ma detrital zircons were likely sourced mostly from the Cathaysia block, as the product of erosion. Occurrence of a great deal of ca. 430 Ma zircons may imply that the erosion in the SCB was intensive. As a result, most of the pegmatites that occurred at the top part of the granite-pegmatite system were eroded away after their formation, and only local limited pegmatites, such as the Nanping pegmatites, survived.

Occurrence of a great amount of pegmatites without outcropping parental granite in Chinese Altay orogen implies that erosion is weak after the formation of granite-pegmatite systems. However, this idea is not supported by the reliable data. Conversely, the metamorphic grade of country rocks of pegmatites in the South China is greenschist facies (Wan et al., 2007). On the other hand, the metamorphic grade of country rocks in the Chinese Altai orogen can reach to granulite facies (Chen et al., 2006; Li et al., 2015, 2010a,b, 2014; Tong et al., 2014). Therefore, in terms of metamorphism, the erosion level in Chinese Altai orogen is deeper than in South China orogen because of the higher metamorphic grade of country rocks in Chinese Altai orogen.

When the fractional crystallization model and subsequent erosion is hard to account for the decoupling of the pegmatite and granite system, an alternative model based on direct crustal anatexis has been proposed to explain the genesis of pegmatites, especially in certain cases where no potential parental granite is observed and the pegmatites are associated with migmatites (Shaw et al., 2016). An increasing number of studies describe granitic pegmatites that are considered to be derived by direct melting rather than by fractional crystallization. Example include the Munchberg Massif, Germany (Franz and Smelik, 1995), the Fraser Lake area of Northern Saskatchewan, Canada (McKechnie et al., 2012), the Moldanubian domain of the Bohemian Massif, Czech Republic (Melleton et al., 2012), and the Lewisian Gnesiss complex of north-west Scotland (Shaw et al., 2016).

The early Paleozoic orogen in the South China exhibits a clockwise pressure–temperature path of metamorphism, and the amphibolites-facies metamorphism occurred between ca. 460 and 445 Ma, whereas cooling below 500–300° occurred by ca. 420 Ma (Li et al., 2010a,b). There is a minimum gap of 30 Ma between metamorphism and the emplacement of rare metal pegmatites (such as Nanping No. 31 pegmatite). Thus a direct genetic relationship of rare metal pegmatites with the metamorphic event is unlikely. Conversely, recent research has shown that pegmatites in Chinese Altay orogen were mainly emplaced from Late Permian to Triassic (Wang et al., 2007; Chen, 2011; Ren et al., 2011; Lv et al., 2012; Ma, 2014), the ages of pegmatite emplacement exhibit a close temporal relationship with the high temperature metamor-

Table 5
Zircon Hf isotopic analytical results of the Nanping No.31 pegmatite.

No.	$^{176}Yb/^{177}Hf$		$^{176}Lu/^{177}Hf$		$^{176}Hf/^{177}UHf$		t(Ma)	$\varepsilon Hf(t)$	T_{DM}	T_{DM2}	$f_{Lu/Hf}$
	Ratio	1σ	Ratio	1σ	Ratio	1σ					
NP31-01	0.008112	0.000111	0.000310	0.0000027	0.282200	0.000009	387	−11.82	1457	2121	−0.99
NP31-02	0.010093	0.000217	0.000372	0.0000047	0.282206	0.000009	387	−11.60	1450	2107	−0.99
NP31-03	0.004938	0.000290	0.000184	0.0000087	0.282167	0.000007	387	−12.94	1497	2192	−0.99
NP31-04	0.010033	0.000089	0.000375	0.0000040	0.282190	0.000006	387	−12.17	1473	2144	−0.99
NP31-05	0.000690	0.000119	0.000026	0.0000043	0.282156	0.000005	387	−13.29	1506	2214	−1.00
NP31-06	0.001119	0.000076	0.000042	0.0000023	0.282194	0.000022	387	−11.94	1454	2129	−1.00
NP31-07	0.001366	0.000097	0.000051	0.0000031	0.282143	0.000004	387	−13.77	1525	2244	−1.00
NP31-08	0.001319	0.000012	0.000045	0.0000004	0.282141	0.000003	387	−13.81	1526	2246	−1.00
NP31-09	0.006258	0.000264	0.000240	0.0000087	0.282166	0.000007	387	−12.99	1500	2194	−0.99

$\varepsilon Hf(t) = ((^{176}Hf/^{177}Hf)_S - (^{176}Lu/^{177}Hf)_S \times (e^{\lambda t} - 1))/((^{176}Hf/^{177}Hf)_{CHUR} - (^{176}Lu/^{177}Hf)_{CHUR} \times (e^{\lambda} - 1))$.
$T_{DM} = 1/\lambda \times Ln[1 + ((^{176}Hf/^{177}Hf)_S - (^{176}Hf/^{177}Hf)_{DM})/((^{176}Lu/^{177}Hf)_S - (^{176}Lu/^{177}Hf)_{DM})]$.
$T_{DM2} = T_{DM} - (T_{DM} - t) \times ((f_{CC} - f_S)/(f_{CC} - f_{DM}))$.
$f_{Lu/Hf} = (^{176}Lu/^{177}Hf)_S/(^{176}Lu/^{177}Hf)_{CHUR} - 1$.
t = 387 Ma; $\lambda = 1.867 \times 10^{-11}$ year^{-1}; the $^{176}Hf/^{177}Hf$ and $^{76}Lu/^{177}Hf$ ratios of chondrite and depleted mantle at the present are 0.282772 and 0.0332, 0.28325 and 0.0384, respectively; $f_{Lu/Hf}$ value of the crust is −0.55.

Table 6
Major element compositions of coltan from the Nanping No. 31 pegmatite.

Oxide	1	2	3	4	5	6	7	8	9	10	11	12	13	14	15	16	17	18	19	20	21	22	23	24	25
Nb_2O_5	44.17	44.04	44.24	43.38	43.86	43.47	44.03	43.61	44.24	43.51	43.94	45.76	45.93	44.86	45.15	44.19	44.26	44.67	45.99	44.41	43.91	42.75	44.59	44.38	44.31
Ta_2O_5	35.05	34.82	35.15	35.69	35.56	35.18	34.76	35.21	36.02	35.21	35.08	33.03	33.95	34.90	35.86	35.83	35.58	34.66	32.80	34.39	35.29	36.62	35.68	35.61	35.55
SnO_2	0.36	0.50	0.45	0.39	0.41	0.44	0.36	0.47	0.39	0.39	0.48	0.37	0.42	0.13	0.46	0.43	0.40	0.45	0.40	0.43	0.45	0.54	0.43	0.44	0.42
TiO_2	0.41	0.41	0.39	0.31	0.38	0.33	0.36	0.36	0.29	0.41	0.39	0.41	0.40	0.34	0.36	0.31	0.39	0.40	0.41	0.38	0.43	0.36	0.34	0.32	0.38
Sc_2O_3	0.17	0.26	0.14	0.27	0.31	0.32	0.10	0.15	0.08	0.09	0.26	0.13	0.23	0.32	0.16	0.20	0.16	0.16	0.23	0.19	0.07	0.12	0.25	0.15	0.17
FeO	11.95	11.68	11.73	11.70	11.88	11.72	11.64	12.07	11.61	11.90	11.83	12.22	12.44	12.48	11.76	11.96	12.06	11.81	12.25	11.89	11.50	11.68	11.78	11.58	11.75
MnO	6.90	6.78	6.74	6.89	6.82	6.91	6.86	6.97	6.85	6.91	6.60	6.72	6.72	6.50	6.98	6.95	6.75	6.79	6.64	6.88	6.71	6.82	6.90	6.78	6.76
Total	99.00	98.48	98.85	98.63	99.22	98.36	98.11	98.84	99.48	98.43	98.57	98.65	100.09	99.53	100.74	99.88	99.60	98.94	98.71	98.57	98.35	98.88	99.97	99.26	99.33

Structural formula calculated on the basis of O = 6 atoms

apfu	1	2	3	4	5	6	7	8	9	10	11	12	13	14	15	16	17	18	19	20	21	22	23	24	25
Nb	1.324	1.326	1.329	1.310	1.314	1.314	1.332	1.313	1.324	1.315	1.323	1.365	1.353	1.334	1.330	1.316	1.321	1.337	1.368	1.334	1.324	1.326	1.329	1.310	1.314
Ta	0.629	0.627	0.632	0.645	0.637	0.636	0.629	0.634	0.645	0.637	0.632	0.589	0.598	0.621	0.632	0.639	0.635	0.621	0.584	0.618	0.629	0.627	0.632	0.645	0.637
Sn	0.010	0.013	0.012	0.010	0.011	0.012	0.010	0.012	0.010	0.010	0.013	0.010	0.011	0.003	0.012	0.011	0.010	0.012	0.010	0.011	0.012	0.013	0.012	0.010	0.011
Ti	0.020	0.020	0.019	0.016	0.019	0.016	0.018	0.018	0.014	0.020	0.020	0.020	0.020	0.017	0.018	0.015	0.019	0.020	0.020	0.019	0.020	0.020	0.019	0.016	0.019
Sc	0.010	0.015	0.008	0.016	0.018	0.018	0.006	0.009	0.005	0.005	0.015	0.008	0.013	0.018	0.009	0.012	0.009	0.009	0.013	0.011	0.010	0.015	0.008	0.016	0.018
Fe	0.659	0.647	0.648	0.650	0.655	0.652	0.648	0.668	0.639	0.662	0.656	0.670	0.674	0.683	0.637	0.656	0.662	0.650	0.670	0.657	0.659	0.647	0.648	0.650	0.655
Mn	0.385	0.380	0.377	0.387	0.381	0.389	0.387	0.391	0.382	0.389	0.370	0.373	0.369	0.360	0.383	0.386	0.375	0.379	0.368	0.385	0.385	0.380	0.377	0.387	0.381
$Ta^\#$	0.32	0.32	0.32	0.33	0.33	0.33	0.32	0.33	0.33	0.33	0.32	0.30	0.31	0.32	0.32	0.33	0.32	0.32	0.30	0.32	0.32	0.34	0.32	0.32	0.32
$Mn^\#$	0.37	0.37	0.37	0.37	0.37	0.37	0.37	0.37	0.37	0.37	0.36	0.36	0.35	0.35	0.38	0.37	0.36	0.37	0.35	0.37	0.37	0.37	0.37	0.37	0.37

All Fe is expressed as Fe^{2+}. $Ta^\# = Ta/(Nb + Ta)$, $Mn^\# = Mn/(Fe + Mn)$. Symbols: Fcl: columbite-(Fe), Ftn: ferrotantalite-(Fe), Mcl: columbite-(Mn), Mtn: tantalite-(Mn).

Table 7
LA-ICP-MS coltan U-Pb analytical results of the Nanping No. 31 pegmatite.

No.	$^{207}Pb/^{206}Pb$		$^{207}Pb/^{235}U$		$^{206}Pb/^{238}U$		$^{207}Pb/^{206}Pb$		$^{207}Pb/^{235}U$		$^{206}Pb/^{238}U$	
	Ratio	1σ	Ratio	1σ	Ratio	1σ	Age(Ma)	1σ	Age(Ma)	1σ	Age(Ma)	1σ
cl-01	0.0555	0.0022	0.4782	0.0178	0.0626	0.0019	432.5	86.6	396.8	12.3	391.6	11.2
cl-02	0.0539	0.0007	0.4660	0.0069	0.0629	0.0015	366.3	30.3	388.4	4.8	392.9	9.4
cl-03	0.0591	0.0008	0.4913	0.0071	0.0604	0.0015	570.9	28.3	405.8	4.8	378.1	9.0
cl-04	0.0540	0.0008	0.4613	0.0071	0.0622	0.0015	368.7	31.4	385.2	4.9	388.7	9.3
cl-05	0.0554	0.0008	0.4689	0.0070	0.0615	0.0015	429.5	30.0	390.5	4.8	384.6	9.2
cl-06	0.0552	0.0007	0.4637	0.0067	0.0610	0.0015	420.3	29.0	386.8	4.7	381.9	9.1
cl-07	0.0534	0.0008	0.4574	0.0070	0.0622	0.0015	347.0	31.9	382.5	4.9	389.0	9.3
cl-08	0.0548	0.0008	0.4742	0.0075	0.0629	0.0016	404.3	33.1	394.1	5.2	393.1	9.4
cl-09	0.0550	0.0017	0.4897	0.0144	0.0646	0.0018	413.5	66.9	404.7	9.8	403.6	10.7
cl-10	0.0567	0.0008	0.4847	0.0072	0.0621	0.0015	477.7	30.0	401.3	4.9	388.3	9.3
cl-11	0.0541	0.0007	0.4702	0.0070	0.0631	0.0016	374.0	30.3	391.3	4.8	394.5	9.5
cl-12	0.0560	0.0008	0.4848	0.0071	0.0629	0.0016	449.9	29.1	401.4	4.9	393.2	9.4
cl-13	0.0582	0.0007	0.4961	0.0069	0.0618	0.0015	537.8	27.6	409.1	4.7	386.7	9.3
cl-14	0.0590	0.0008	0.4933	0.0074	0.0606	0.0015	568.2	29.8	407.1	5.0	379.5	9.1
cl-15	0.0584	0.0008	0.5076	0.0073	0.0631	0.0016	544.1	28.1	416.9	4.9	394.3	9.5
cl-16	0.0568	0.0008	0.4897	0.0072	0.0625	0.0016	483.8	29.4	404.7	4.9	390.9	9.4
cl-17	0.0563	0.0007	0.4721	0.0069	0.0609	0.0015	462.6	29.0	392.6	4.7	380.8	9.2
cl-18	0.0575	0.0008	0.4834	0.0074	0.0609	0.0015	511.8	31.4	400.4	5.1	381.3	9.2
cl-19	0.0569	0.0008	0.4670	0.0068	0.0595	0.0015	488.7	29.0	389.1	4.7	372.5	9.0
cl-20	0.0573	0.0008	0.4882	0.0073	0.0618	0.0015	503.6	29.8	403.7	5.0	386.4	9.3
cl-21	0.0584	0.0017	0.4962	0.0141	0.0617	0.0017	543.6	63.9	409.1	9.6	385.6	10.3

phism (such as granulite-facies metamorphism). This metamorphism results in the devolatilization of the lower curst, producing fluids enriched in F, Li and other rare elements, and these fluids would induce a limited degree of partial melting of an unknown protolith in the middle crust. The melts would then be collected and channeled along vertical structures in the upper crust. A similar model has been proposed by Melleton et al. (2012) for the formation of LCT pegmatites in the Moldanubian domain of Bohemian Massif, Czech Republic.

Combining our age data with the previous data, although the paternal granites have not been identified yet, pegmatites in the South China Block suggest an origin by extreme magmatic fractionation, on the other hand, pegmatites in Chinese Altay orogen are contemporaneous with high temperature metamorphism and imply an origin by anatexis. However, in order to confirm one or the other model, further investigations of geochemical and isotopic signatures of the migmatites, unmelted sedimentary units, granitic intrusive and pegmatites are necessary.

6. Conclusions

(1) Columbite-group minerals from zone I in the Nanping No. 31 pegmatite vein belong to columbite-(Fe). The compositions and texture features of zircon grains from the same zone identify their magmatic origin.
(2) LA-ICPMS U-Pb dating of columbite-(Fe) and zircon reveal that the emplacement of the Nanping pegmatites occurred at approximately 387 Ma;
(3) Hf isotopic data suggest that the Nanping pegmatite-forming melts are derived from the Paleoproterozoic metasedimentary rocks and the differences in the emplacement age and Hf isotopic features preclude the Xiqin and Jinlong granitic plutons as the parental source of these pegmatites.

Acknowledgments

References

Aldrich, L., Davis, G., Tilton, G., Wetherill, G., 1956. Radioactive ages of minerals from the Brown Derby Mine and the Quartz Creek Granite near Gunnison, Colorado. J. Geophys. Res. 61, 215–232.

Andersen, T., 2002. Correction of common lead in U-Pb analyses that do not report ^{204}Pb. Chem. Geol. 192, 59–79.

Baumgartner, R., Romer, R.L., Moritz, R., Sallet, R., Chiaradia, M., 2006. Columbite-tantalite-bearing granitic pegmatites from the Seridó Belt, Northeastern Brazil: genetic constraints from U-Pb dating and Pb isotopes. Can. Mineral. 44, 69–86.

Blichert-Toft, J., Albarède, F., 1997. The Lu-Hf isotope geochemistry of chondrites and the evolution of the mantle-crust system. Earth Planet. Sci. Lett. 148, 243–258.

Cai, D.-W., Tang, Y., Zhang, H., Lv, Z.-H., Liu, Y.-L., 2016. Petrogenesis and tectonic setting of the Devonian Xiqin A-type granite in the northeastern Cathaysia Block SE China. J. Asian Earth Sci. http://dx.doi.org/10.1016/j.jseaes.2016.05.015. in press.

Cameron, E.N., 1949. Internal structure of granitic pegmatites: economic geology, monograph 2.

Černý, P., 1991a. Fertile granites of precambrian rare-element pegmatite fields: is geochemistry controlled by tectonic setting or source lithologies? Precambr. Res. 51, 429–468.

Černý, P., 1991b. Rare-element granite pegmatites. Part II. Regional to global environments and petrogenesis. Geosci. Canada 18, 68–81.

Černý, P., 1991c. Rare-element granite pegmatites: Part I. Anatomy and internal evolution of pegmatite deposits. Geosci. Canada 18, 49–67.

Černý, P., 1992. Geochemical and petrogenetic features of Mineralization in rare-element granitic pegmatites in the light of current research. Appl. Geochem. 7, 393–416.

Černý, P., Ercit, T.S., 2005. The classification of granitic pegmatites revisited. Can. Mineral. 43, 2005–2026.

Černý, P., Meintzer, R.E., Anderson, A.J., 1985. Extreme fractionation in rare-element granitic pegmatites; selected examples of data and mechanisms. Can. Mineral. 23, 381–421.

Charvet, J., 2013. The Neoproterozoic-early Paleozoic tectonic evolution of the south China block: an overview. J. Asian Earth Sci. 74, 198–209.

Charvet, J., Shu, L.-S., Shi, Y.-S., Guo, L.-Z., Faure, M., 1996. The building of south China: collision of Yangzi and Cathaysia blocks, problems and tentative answers. J. SE Asian Earth Sci. 13, 223–235.

Charvet, J., Shu, L.-S., Faure, M., Choulet, F., Wang, B., Lu, H.f., Breton, N.L., 2010. Structural development of the lower Paleozoic belt of south China: genesis of an intracontinental orogen. J. Asian Earth Sci. 39, 309–330.

Che, X.-D., Wu, F.-Y., Wang, R.-C., Gerdes, A., Ji, W.-Q., Zhao, Z.-H., Yang, J.-H., Zhu, Z.-Y., 2015. In situ U-Pb isotopic dating of columbite–tantalite by LA-ICP-MS. Ore Geol. Rev. 65 (4), 979–989.

Chen, H.-L., Yang, S.-F., Li, Z.-L., Yu, X., Xiao, W.-J., Yuan, C., Lin, X.-B., Li, J.-L., 2006. Zircon SHRIMP U-Pb chronology of fuyun basic granulite and its tectonic significance in altaid orogenic belt. Acta Petrol. Sinica 22, 1351–1358. in Chinese with English Abstract.

Chen, J.-F., 2011. Geochemistry of the plate part in Altai No. 3 pegmatite and its formation and evolution. Graduate University of Chinese Academy of Sciences, Beijing.

Cherniak, D.J., Watson, E.B., 2003. Diffusion in Zircon. Rev. Mineral. Geochem. 53, 113–143.

Deng, X.-D., Li, J.-W., Zhao, X.-F., Hu, Z.-C., Hu, H., Selby, D., de Souza, Z.S., 2013. U-Pb isotope and trace element analysis of columbite-(Mn) and zircon by laser ablation ICP–MS: implications for geochronology of pegmatite and associated ore deposits. Chem. Geol. 344, 1–11.

Dewaele, S., Henjes-Kunst, F., Melcher, F., Sitnikova, M., Burgess, R., Gerdes, A., Fermamdez, M.A., Clercq, F.D., Muchez, P., Lehmann, B., 2011. Late Neoproterozoic overprinting of the cassiterite and columbite-tantalite bearing pegmatites of the Gatumba area, Rwanda (central Africa). J. Afr. Earth Sci. 61, 10–26.

Dill, H.G., 2015. Pegmatites and aplites: their genetic and applied ore geology. Ore Geol. Rev. 69, 417–561.

Dill, H.G., Gerdes, A., Weber, B., 2007. Cu-Fe-U phosphate mineralization of the Hagendorf-Pleystein pegmatite province, Germany: with special reference to laser-ablation inductively-coupled plasma mass spectrometry (LA-ICP-MS) of limonite-cored torbernite. Mineral. Mag. 71, 371–387.

Faure, M., Shu, L.-S., Wang, B., Charvet, J., Choulet, F., Monie, P., 2009. Intracontinental subduction: a possible mechanism for the early palaeozoic orogen of SE China. Terra Nova 21, 360–368.

Geisler, T., Schaltegger, U., Tomaschek, F., 2007. Re-equilbration of zircon in aqueous fluids and melts. Elements 3, 43–50.

Franz, G., Smelik, E.A., 1995. Zoisite-clinozoisite bearing pegmatites and their importance for decompressional melting in eclogites. Eur. J. Mineral. 7, 1421–1436.

Griffin, W.L., Wang, X., Jackson, S.E., Pearson, N.J., O'Reilly, S.Y., Xu, X., Zhou, X.-M., 2002. Zircon chemistry and magma mixing, SE China: In-situ analysis of Hf isotopes, Tonglu and Pingtan igneous complexes. Lithos 61, 237–269.

Hoskin, P.W.O., 2005. Trace-element composition of hydrothermal zircon and the alteration of hadean zircon from the Jack Hills, Australia. Geochim. Cosmochim. Acta 69, 637–648.

Hoskin, P.W.O., Schaltegger, U., 2003. The composition of zircon and igneous and metamorphic petrogenesis. Rev. Mineral. Geochem. 53, 27–62.

Hu, Z., Liu, Y., Gao, S., Liu, W., Zhang, W., Tong, X., Lin, L., Zong, K., Li, M., Chen, H., Zhou, L., Yang, L., 2012. Improved in situ Hf isotope ratio analysis of zircon using newly designed X skimmer cone and jet sample cone in combination with the addition of nitrogen by laser ablation multiple collector ICP-MS. J. Anal. At. Spectrom. 27, 1391–1399.

Jackson, S.E., Pearson, N.J., Griffin, W.L., Belousova, E.A., 2004. The application of laser ablation-inductively coupled plasma-mass spectrometry to in situ U-Pb zircon geochronology. Chem. Geol. 211, 47–69.

Jahns, R.H., Burnham, C.W., 1969. Experimental studies of pegmatite genesis: l. A model for the derivation and crystallization of granitic pegmatites. Econ. Geol. 64, 843–864.

Kinny, P.D., Maas, R., 2003. Lu-Hf and Sm-Nd isotope systems in zircon. Rev. Mineral. Geochem. 53, 327–341.

Landes, K.K., 1933. Origin and classification of pegmatites. Am. Mineral. 18, 33–56.

Li, P.-F., Yuan, C., Sun, M., Long, X.-P., Cai, K.-D., 2015. Thermochronological constraints on the late Paleozoic tectonic evolution of the southern Chinese Altai. J. Asian Earth Sci. 113, 51–60.

Li, Z.-X., Li, X.-H., Wartho, J.A., Clark, C., Li, W.-X., Zhang, C.-L., Bao, C.-M., 2010a. Magmatic and metamorphic events during the early Paleozoic Wuyi-Yunkai orogeny, southeastern south China: new age constraints and pressure-temperature conditions. Geol. Soc. Am. Bull. 122, 772–793.

Li, Z.-L., Li, Y.-Q., Chen, H.-L., Santosh, M., Xiao, W.-J., Wang, H.-H., 2010b. SHRIMP U-Pb zircon chronology of ultrahigh-temperature spinel-orthopyroxene-garnet granulite from South Altay orogenic belt, northwestern China. Island Arc 19, 506–516.

Li, Z.-L., Yang, X.-Q., Li, Y.-Q., Santosh, M., Chen, H.-L., Xiao, W.-J., 2014. Late Paleozoic tectono–metamorphic evolution of the Altai segment of the central

Asian orogenic belt: constraints from metamorphic P-T pseudosection and zircon U-Pb dating of ultra-high-temperature granulite. Lithos 204, 83–96.

Liu, Y., Hu, Z., Gao, S., Günther, D., Xu, J., Gao, C., Chen, H., 2008. In situ analysis of major and trace elements of anhydrous minerals by LA-ICP-MS without applying an internal standard. Chem. Geol. 257, 34–43.

London, D., 2005. Granitic pegmatites: an assessment of current concepts and directions for the future. Lithos 80, 281–303.

London, D., 2008. Pegmatites. In: Martin, R.F. (Ed.), The Canadian Mineralogist Special Publication 10. Mineralogical Association of Canada, Quebec.

London, D., 2009. The origin of primary textures in granitic pegmatites. Can. Mineral. 47, 697–724.

London, D., 2014. A petrologic assessment of internal zonation in granitic pegmatites. Lithos 184–187, 74–104.

Ludwing, K., 2003. User's Manual for Isoplot 3.00. A Geochronological Toolkit for Microsoft Excel, vol. 4. Berkeley Geochronology Center, Berkeley, CA, pp. 1–70.

Lv, Z.-H., Zhang, H., Tang, Y., Guan, S.-J., 2012. Petrogenesis and magmatic–hydrothermal evolution time limitation of Kelumute No. 112 pegmatite in Altay, Northwestern China: evidence from zircon UPb and Hf isotopes. Lithos 154, 374–391.

Ma, Z.-L., 2014. Zircon U-Pb dating and hf isotopes of pegmatites from the kaluan mining area in the Altay, Xinjiang and their genetic relationship with the halong granite. Graduate University of Chinese Academy of Sciences, Beijing.

McKechnie, C.L., Annesley, I.R., Ansdell, K.M., 2012. Medium- to low-pressure pelitic gneisses of Graser Lakes Zone B, Wollaston Domain, Northern Saskatchewan, Canada: mineral compositions, metamophic P-T-t path, and implications for the genesis of radioactive abyssal granitic pegmatites. Can. Mineral. 50, 1669–1694.

McDonough, W.F., Sun, S.-s., 1995. The composition of the Earth. Chem. Geol. 120, 223–253.

Melleton, J., Gloaguen, E., Frei, D., Novák, M., Breiter, K., 2012. How are the emplacement of rare-element pegmatites, regional metamorphism and magmatism interrelated in the Moldanubian Domain of the Variscan Bohemian Massif, Czech Republic? Can. Mineral. 50, 1751–1773.

Meng, L., Li, Z.-X., Chen, H., Li, X.-H., Zhu, C., 2015. Detrital zircon U-Pb geochronology, Hf isotopes and geochemistry constraints on crustal growth and Mesozoic tectonics of southeastern China. J. Asian Earth Sci. 105, 286–299.

Qiu, N.-M., Yang, Y.-Q., 1985. Nanping Granitic Pegmatite (in Chinese with English abstract).

Rao, C., Wang, R.-C., Hatert, F., Gu, X.P., Ottolini, L., Hu, H., Dong, C.-W., Bo, F.D., Baijot, M., 2014a. Strontiohurlbutite, SrBe$_2$(PO$_4$)$_2$, a new mineral from Nanping No. 31 pegmatite, Fujian Province Southeastern China. Am. Mineral. 99, 494–499.

Rao, C., Wang, R.-C., Hatert, F., Baijot, M., 2014b. Hydrothermal transformations of triphylite from the Nanping No. 31 pegmatite dyke, southeastern China. Eur. J. Mineral. 26, 179–188.

Rao, C., Wang, R.-C., Hu, H., 2011. Paragenetic assemblages of beryllium silicates and phosphates from the Nanping No. 31 granitic pegmatite dyke, Fujian Province Southeatern China. Can. Mineral. 49, 1175–1187.

Rao, C., Wang, R.-C., Hu, H., Zhang, W.-L., 2009. Complex internal textures in oxide minerals from the Nanping No. 31 dyke of granitic pegmatite, Fujian Province southeastern China. Can. Mineral. 47, 1195–1212.

Rao, C., Wang, R.-C., Zhang, A.C., Hu, H., 2012. The corundum + tourrmaline nodules related to hydrothermal alteration of spodumene in the Nanping No. 31 pegmatite dyke, Fujian Province southeastern China. Can. Mineral. 50, 1623–1635.

Ren, B.-Q., Zhang, H., Tang, Y., Lv, Z.-H., 2011. LA-ICPMS U-Pb zircon geochronology of the Altai pegmatites and its geological significance. Acta Mineral. Sinica 31, 587–596 (in Chinese with English abstract).

Romer, R.L., Lehmann, B., 1995. U-Pb columbite age of Neoproterozoic Ta-Nb mineralization in Burundi. Econ. Geol. 90, 2303–2309.

Romer, R.L., Smeds, S.-A., 1994. Implications of U-Pb ages of columbite-tantalites from granitic pegmatites for the Palaeoproterozoic accretion of 1.90–1.85 Ga magmatic arcs to the baltic shield. Precambr. Res. 67, 141–158.

Romer, R.L., Smeds, S.-A., 1996. U-Pb columbite ages of pegmatites from Sveconorwegian terranes in southwestern Sweden. Precambr. Res. 76, 15–30.

Romer, R.L., Smeds, S.-A., 1997. U-Pb columbite chronology of post-kinematic palaeoproterozoic pegmatites in Sweden. Precambr. Res. 82, 85–99.

Shaw, R.A., Goodenough, K.M., Roberts, N.M.W., Horstwood, M.S.A., Chenery, S.R., Gunn, A.G., 2016. Petrogenesis of rare-metal pegmatites in high-grade metamorphic terranes: a case study from the lewisian gneiss complex of north-west Scotland. Precambr. Res. 281, 338–362.

Söderlund, U., Patchett, P.J., Vervoort, J.D., Isachsen, C.E., 2004. The ^{176}Lu decay constant determined by Lu–Hf and U–Pb isotope systematics of Precambrian mafic intrusions. Earth Planet. Sci. Lett. 219, 311–324.

Selway, J.B., Breaks, F.W., Tindle, A.G., 2005. A review of rare-element (LI-CS-TA) pegmatite exploration techniques for the superior province, Canada, and large worldwide tantalum deposits. Explor. Min. Geol. 14, 1–30.

Shu, L.-S., Faure, M., Yu, J.-H., Jahn, B.-M., 2011. Geochronological and geochemical features of the Cathaysia block (south China): new evidence for the Neoproterozoic breakup of Rodinia. Precambr. Res. 187, 263–276.

Shu, L.-S., Jahn, B.M., Charvet, J., Santosh, M., Wang, B., Xu, X.-S., Jiang, S.-Y., 2014. Early Paleozoic depositional environment and intraplate tectono-magmatism in the Cathaysia Block (south China): evidence from stratigraphic, structural, geochemical and geochronological investigations. Am. J. Sci. 314, 154–186.

Shu, L.-S., Faure, M., Wang, B., Zhou, X., Song, B., 2008. Late Palaeozoic–Early Mesozoic geological features of south China: response to the Indosinian collision events in southeast Asia. C. R. Geosci. 340, 151–165.

Shu, L.-S., Faure, M., Jiang, S.-Y., Yang, Q., Wang, Y., 2006. SHRIMP zircon U-Pb age, litho-and biostratigraphic analyses of the Huaiyu domain in South China. Episodes 29, 244–252.

Shu, L.-S., Wang, B., Cawood, P.A., Santosh, M., Xu, Z.-Q., 2015. Early Paleozoic and Early Mesozoic intraplate tectonic and magmatic events in the Cathaysia block south China. Tectonic, 1600–1621.

Shu, L.-S., Zhou, X.-M., Deng, P., Wang, B., Jiang, S.-Y., Yu, J.-H., Zhao, X.-X., 2009. Mesozoic tectonic evolution of the Southeast China Block: new insights from basin analysis. J. Asian Earth Sci. 34, 376–391.

Simmons, W.B.S., Webber, K.L., 2008. Pegmatite genesis: state of the art. Eur. J. Mineral. 20, 421–438.

Smith, S.R., Foster, G.L., Romer, R.L., Tindle, A.G., Kelley, S.P., Noble, S.R., Horstwood, M., Breaks, F.W., 2004. U-Pb columbite-tantalite chronology of rare-element pegmatites using TIMS and Laser Ablation-Multi Collector-ICP-MS. Contrib. Mineral. Petrol. 147, 549–564.

Song, M.-J., Shu, L.-S., Santosh, M., Li, J.-Y., 2015. Late Early Paleozoic and Early Mesozoic intracontinental orogeny in the South China Craton: Geochronological and geochemical evidence. Lithos 232, 360–374.

Song, M.-J., Shu, L.-S., Santosh, M., 2016. Early Mesozoic granites in the Nanling Belt, South China: implications for intracontinental tectonics associated with stress regime transformation. Tectonophysics 676, 148–169.

Tong, L.-X., Xu, Y.-G., Cawood, P.A., Zhou, X., Chen, Y.-B., Liu, Z., 2014. Anticlockwise P-T evolution at ~280 Ma recorded from ultrahigh-temperature metapelitic granulite in the Chinese Altai orogenic belt, a possible link with the Tarim mantle plume? J. Asian Earth Sci. 94, 1–11.

Wan, Y.-S., Liu, D.-Y., Xu, M.-H., Zhuang, J.-M., Song, B., Shi, Y.-R., Du, L.-L., 2007. SHRIMP U-Pb zircon geochronology and geochemistry of metavolcanic and metasedimentary rocks in Northwestern Fujian, Cathaysia block, China: Tectonic implications and the need to redefine lithostratigraphic units. Gondwana Res. 12, 166–183.

Wang, T., Jahn, B.-M., Kovach, V.P., Tong, Y., Wilde, S.A., Hong, D-W., Li, S., Salnikova, E.B., 2014. Mesozoic intraplate granitic magmatism in the Altai accretionary orogen, NW China: Implications for the orogenic architecture and crustal growth. Am. J. Sci. 314, 1–42.

Wang, T., Tong, Y., Jahn, B.-M., Zou, T.-R., Wang, Y.-B., Hong, D.-W., Han, B.-F., 2007. SHRIMP U-Pb Zircon geochronology of the Altai No. 3 pegmatite, NW China, and its implications for the origin and tectonic setting of the pegmatite. Ore Geol. Rev. 32, 325–336.

Wang, Y.-J., Fan, W.-M., Zhang, G.-W., Zhang, Y.-H., 2013. Phanerozoic tectonics of the South China Block: key observations and controversies. Gondwana Res. 23, 1273–1305.

Wang, Y.-J., Zhang, A.-M., Fan, W.-M., Zhao, G.-C., Zhang, G.-W., Zhang, Y.-Z., Zhang, F.-F., Li, S.-Z., 2011. Kwangsian crustal anatexis within the eastern South China Block: Geochemical, zircon U-Pb geochronological and Hf isotopic fingerprints from the gneissoid granites of Wugong and Wuyi-Yunkai Domains. Lithos 127, 239–260.

Yan, C., Shu, L.-S., Santosh, M., Yao, J.-L., Li, J.-Y., Li, C., 2015. The Precambrian tectonic evolution of the western Jiangnan Orogen and western Cathaysia Block: evidence from detrital zircon age spectra and geochemistry of clastic rocks. Precambr. Res. 268, 33–60.

Yang, Y.-Q., Ni, Y.-X., Guo, Y.-Q., Qiu, N.M., Chen, C.H., Cai, C.F., Zhang, Y.-P., Liu, J.-B., Chen, Y.-X., 1987. Rock-forming and ore-forming characteristics of the Xikeng granitic pegmaites in Fujian Province. Min. Deposits 6, 10–21 (in Chinese with English abstract).

Yao, J.-L., Shu, L.-S., Santosh, M., 2014. Neoproterozoic arc-trench system and breakup of the South China Craton: constraints from N-MORB type and arc-related mafic rocks, and anorogenic granite in the Jiangnan orogenic belt. Precambr. Res. 247, 187–207.

Yao, J.-L., Shu, L.-S., Santosh, M., Li, J.-Y., 2015. Neoproterozoic arc-related andesite and orogeny-related unconformity in the eastern Jiangnan orogenic belt: constraints on the assembly of the Yangtze and Cathaysia blocks in South China. Precambr. Res. 62, 84–100.

Yuan, H.-L., Gao, S., Dai, M.-N., Zong, C.-L., Günther, D., Fontaine, G.-H., Liu, X.-M., Diwu, C.-R., 2008. Simultaneous determinations of U-Pb age, Hf isotopes and trace element compositions of zircon by excimer laser-ablation quadrupole and multiple-collector ICP-MS. Chem. Geol. 247, 100–118.

Zagorsky, V.Y., Vladimirov, A.G., Makagon, V.M., Kuznetsova, L.G., Smirnov, S.Z., D'yachkov, B.A., Annilova, I.Y., Shokalsky, S.P., Uvarov, A.N., 2014. Large fields of spodumene pegmatites in the settings of rifting and postcollisional shear-pull-apart dislocations of continental lithosphere. Russ. Geol. Geophys. 55, 237–251.

Zhang, A.-C., Wang, R.-C., Hu, H., Chen, X.-M., Zhang, H., 2004a. Occurrences of foitite and rossmanite from the Koktokay no. 3 granitic pegmatite dyke, Altai, northwestern China: A record of hydrothermal fluids. Can. Mineral. 42, 873–882.

Zhang, A.-C., Wang, R.-C., Hu, H., Zhang, H., Zhu, J.-C., Chen, X.-M., 2004b. Chemical evolution of Nb-Ta oxides and zircon from the Koktokay No. 3 granitic pegmatite, Altai, northwestern China. Mineral. Mag. 68, 739–756.

Zhang, A.-C., Wang, R.-C., Jiang, S.-Y., Hu, H., Zhang, H., 2008. Chemical and textural features of tourmaline from the spodumene-subtype Koktokay No. 3 pegmatite, Altai, northwestern China: A record of magmatic to hydrothermal evolution. Can. Mineral. 46, 41–58.

Zhang, F.-F., Wang, Y.-J., Zhang, A.-M., Fan, W.-M., Zhang, Y.-Z., Zi, J.-W., 2012. Geochronological and geochemical constraints on the petrogenesis of middle Paleozoic (Kwangsian) massive granites in the eastern south China Block. Lithos 150, 188–208.